Identification of Inelastic Parameters of the AISI 304 Stainless Steel

Miguel Vaz Jr., E. R. Hulse and M. Tomiyama

Abstract A proper choice of inelastic parameters is one of the most important aspects for a successful simulation of metal forming processes. Several issues must be observed when choosing such parameters, amongst which the compatibility between the magnitude of the plastic deformation of the target forming operation and the mechanical test employed to obtain those parameters. Within this context, the present work addresses the suitability of selected phenomenological hardening models and identification of the corresponding inelastic parameters based on curve-fitting strategies (logarithmic-based equations) and optimization methods (non-logarithmic models) for the AISI 304 austenitic stainless steel. Tensile tests were performed using specimens of different sizes. Based on a combined assessment of all types of specimens, it was observed that the curve-fitting technique was able to describe with excellent accuracy deformations up to maximum load. In order to contemplate larger plastic deformations, an inverse problem strategy based on optimization methods was used to account for material response up to macroscopic failure of the specimens. Numerical simulation of the tensile tests shows that the latter technique associated with non-logarithmic hardening equations provided the best approximation to the experimental data.

1 Introduction

Austenitic stainless steels are the most widely used type of corrosion-resistant steels. This class of steels are generally characterized by containing low levels of Carbon and high levels of Chromium and Nickel. In addition to Cr and Ni, other elements

M. Vaz Jr. (✉) · E. R. Hulse · M. Tomiyama
State University of Santa Catarina, Campus Universitário Prof. Avelino Marcante, Joinville 89219-710, Brazil
e-mail: Miguel.Vaz@udesc.br

E. R. Hulse
e-mail: emilio.r.hulse@embraco.com

M. Tomiyama
e-mail: masahiro.tomiyama@udesc.br

A. Öchsner and H. Altenbach (eds.), *Engineering Design Applications II*,
Advanced Structured Materials 113, https://doi.org/10.1007/978-3-030-20801-1_2

may be added in order to confer specific properties and characteristics to the material, e.g. Molybdenum to increase pitting resistance, Phosphorus and Sulphur to improve machinability, Selenium for better machined surfaces, Boron to enhance the steel capacity to absorb neutrons in nuclear thermal reactors, Silicon for higher heat resistance and Copper to improve cold working, amongst other elements [1]. The stainless steel AISI 304 is the most used grade due to its combination of mechanical (formability and weldability) and chemical (corrosion and oxidation resistance) characteristics.

The good formability of the type 304 stainless steel is associated with its relatively low yield stress and high ductility, thereby allowing large plastic deformation before onset of mechanical failure. Such features favour cold working processing [2] (roll forming, deep drawing, etc.), making possible to manufacture with greater efficiency a wide range of products and components, including consumer items, architectural elements and industrial equipment. Therefore, a proper description of mechanical properties is highly significant to industries, especially when using computational packages to simulate metal forming operations (the user must provide actual inelastic parameters). This work is inserted in this context, aiming to contribute to the discussion by assessing the suitability of some selected phenomenological equations to model hardening evolution and alternative strategies to obtain the corresponding parameters.

Form the viewpoint of tool design and prediction of manufacturing costs, including the modern concept of energy accountability, the issues briefly discussed in the previous paragraph highlights the necessity to develop a methodology to determine material parameters. Material parameters describe different aspects of the nature of the material, ranging from mechanical and thermal behaviour to chemical kinetics. The strategy addressed in this work is primarily concerned with mechanical parameters in association with inelastic deformation.

The literature shows an increasing number of works discussing strategies to determine different types of inelastic parameters, which in turn are associated with the material constitutive relation (plastic, viscoplastic, etc.) and purpose of the analysis itself (hardening, damage, etc.). Techniques based on *curve fitting* and *optimization methods* have been largely adopted in this class of problems. For instance, the suitability of selected hardening equations to describe plastic deformation of ductile materials was addressed by Samuel and co-workers [3, 4]. The authors studied several ductile materials, amongst which the AISI 316L stainless steel, and used a *curve-fitting technique* up to instability onset to obtain the hardening parameters. One of the relevant works on the application of *optimization methods* to obtain hardening parameters was presented by Ponthot and Kleinermann [5]. The study is mostly focused on mathematical aspects of several gradient-based optimization schemes. The authors proposed application in cascade of optimization methods to identification of hardening parameters of the ASTM A533, Grade B, Class 1 low alloy steel based on tensile tests.

A discussion on the hardening behaviour and a proposal of a new phenomenological hardening equation were presented by Dimatteo et al. [6] for Dual Phase (DP) 450/600/800/1000 and Transformation Induced Plasticity (TRIP) 800 steels.

A *curve-fitting strategy* associated with tensile tests was adopted to determine the hardening parameters of a new 3rd order logarithmic yield stress curve. The validation procedure indicated excellent correlation of the engineering stress and strain curves up to maximum load. Noticeably, the present work also investigates the suitability of the hardening equation proposed by Dimatteo et al. [6] to describe isothermal hardening evolution for the AISI 304 stainless steel. A parameter identification technique using *optimization methods* was used by Vaz Jr. et al. [7] to obtain hardening and fracture parameters of low Carbon AISI 1020 steel. The authors discussed application of hybrid optimization strategies and described an experimental-numerical scheme to determine inelastic parameters for two damage constitutive relations.

The brief review presented in the previous paragraphs is not exhaustive and intends to illustrate some of the existing approaches regarding the nature of the inelastic parameters and methodology of parameter identification. It is important to mention that other relevant investigations on the subject are discussed later in the appropriate sections. The present work addresses the suitability of selected phenomenological hardening models and identification of the corresponding inelastic parameters based on *curve-fitting strategies* (logarithmic-based equations) and *optimization methods* (non-logarithmic models) for the AISI 304 stainless steel. The chapter is organized as follows: Section 2 introduces a discussion on logarithmic-based phenomenological hardening equations and its intrinsic association with curve-fitting procedures. Section 3 presents alternative, non-logarithmic hardening equations and an optimization-based strategy to obtain the corresponding hardening parameters. Application of both parameter identification techniques is discussed in Sect. 4 based on tensile tests using specimens of different sizes prepared according to two different technical standards. The main conclusions and remarks are summarised in Sect. 5.

2 Phenomenological Hardening Equations and Curve Fitting Strategies

Tensile tests associated with curve fitting strategies have largely been adopted to determine yield stress parameters for metal materials. In addition to its simplicity, this technique makes possible to directly correlate *true stresses* and *true strains*, thereby conferring a straightforward physical significance. For the sake of objectivity, the reader is referred to Davis [8] for a detailed description of the method, including experimental considerations and requirements. Notwithstanding, it is relevant to emphasise that logarithmic true strains and true stresses represent the actual state of the material and are derived by considering the actual area and length of the specimen as well as constant volume during plastic deformation. The assumption of uniform deformation required by this method restricts evaluation of strains and stresses up to necking (instability) onset. The curve fitting technique is particularly significant when determining the material parameters based on specimens of different sizes. This strategy evinces eventual measurement discrepancies: in spite of different

levels of tensile loads (owing to different cross-sectional areas), the true stress strain curves for each test must show very close approximation up to maximum load.

The literature shows a wide range of empirical equations to describe the yield stress based on logarithmic, $(\ln\sigma) \times (\ln\varepsilon)$ curves. This work addresses yield stress described by the classical Swift's equation [9] and alternative approaches, such as the double-n Swift [10] and a third-order logarithmic polynomial curve [6] (referred here also as cubic logarithmic equation).

One of the most well-known yield stress equation is due to Swift [9]. The author addressed mathematically the conditions for instability of plastic strains based on the Mises-Henky constitutive model. The instability conditions were demonstrated for a strain-hardening material described by the empirical relation

$$\sigma_Y = k\left(\bar{\varepsilon}_p + \varepsilon_0\right)^n, \tag{1}$$

where σ_Y is the yield stress, $\bar{\varepsilon}_p$ is the equivalent plastic strain, k is known as strength coefficient, n is the strain-hardening exponent, and ε_0 is an initial measure of the plastic state of the material (referred here as initial strain). The fitting constants k and n can be easily determined from double logarithm plot of the experimental true stress-strain data within the envelope comprised by the elastic deformation and onset of plastic instability (maximum load). The initial strain, ε_0, is obtained by the intersection of the uniaxial elastic and plastic curves, $\sigma_0 = E\varepsilon_0 = k\varepsilon_0^n$, so that $\varepsilon_0 = (E/k)^{1/(n-1)}$, where σ_0 is the initial yield stress and E is the Young's modulus.

Further modifications of Eq. (1) have been proposed to accommodate non-linear variations of the hardening evolution. Hertelé et al. [10] highlight the fact that two-stage hardening has been observed in various types of metals, including stainless steels. The authors proposed a strategy based on the Ramberg-Osgood equation and presented results for the DIN 1.4462 duplex stainless steel. Kashyap et al. [11, 12] adopted two and three stages of the Holloman relation, $\sigma_Y = k\varepsilon^n$, to describe the behaviour of the AISI 316L stainless steel under high temperature.

In the present work, a double-n Swift curve is investigated, so that

$$\sigma_Y = \begin{cases} k_1(\bar{\varepsilon}_p + \varepsilon_0)^{n_1} & \text{if} \quad \bar{\varepsilon}_p \leqslant \bar{\varepsilon}_p^T \\ k_2(\bar{\varepsilon}_p + \varepsilon_0)^{n_2} & \text{if} \quad \bar{\varepsilon}_p > \bar{\varepsilon}_p^T \end{cases}, \tag{2}$$

in which k_1 and k_2 are the strength coefficients of each stage, n_1 and n_2 are the corresponding hardening indices, $\varepsilon_0 = (E/k_1)^{1/(n_1-1)}$ is the initial strain, and $\varepsilon_p^T = \varepsilon^T - \varepsilon_0 = \exp[\ln(k_1/k_2)/(n_2 - n_1)] - \varepsilon_0$ is the transitional equivalent plastic strain.

The material parameters (k_1, n_1) and (k_2, n_2) of Eq. (2) can be obtained from a double logarithmic plot of the experimental true stress-true strain data based on the assumption of uniform plastic deformation. The key aspect of the double-n Swift curve is the proper computation of the transition point. In this work, the transition between curves "1" and "2" is determined by minimizing a combination of the fitting errors of both hardening stages when determining parameters (k_1, n_1) and (k_2, n_2) (the technique makes use of a simple line search method which maximizes

the average coefficient of determination, $\overline{R}^2(\varepsilon^T) = (R_1^2 + R_2^2)/2$, of curves "1" and "2"). It is also important to note that, contrasting to other empirical equations, the material parameters k and n of the Swift and double-n Swift curves provide a strong physical and technological significance. The strength coefficient, k, directly indicates the magnitude of the forces involved in forming operations, whereas the value of the hardening exponent, n, points out preferred forming processes according to its level.

Within the framework of empirical descriptions of plastic deformation, Dimatteo et al. [6] proposed use of a 3rd order $(\ln\sigma) \times (\ln\varepsilon)$ polynomial fit to DP and TRIP steels in an attempt to predict the influence of alloying elements and heat treatment conditions in a simple manner. This work investigates a possible extension of the applicability range to the AISI 304 stainless steel. In the present study, provision for the elastic envelope is also included, so that

$$\ln(\sigma_Y) = A[\ln(\bar{\varepsilon}_p + \varepsilon_0)]^3 + B[\ln(\bar{\varepsilon}_p + \varepsilon_0)]^2 + C[\ln(\bar{\varepsilon}_p + \varepsilon_0)] + D, \tag{3}$$

where A, B, C, and D are the model parameters to be determined by the curve fitting procedure. Similarly to Swift's equation, the initial strain, ε_0, is obtained by the intersection between the uniaxial elastic and plastic curves and solving the cubic equation, $A[\ln(\varepsilon_0)]^3 + B[\ln(\varepsilon_0)]^2 + (C-1)[\ln(\varepsilon_0)] + [D - \ln(E)] = 0$, for the initial strain.
Remark (i): The curve fitting procedures seek the best approximation under uniaxial stress conditions. Therefore, a combination of such strategy and the aforementioned hardening equations does not guarantee a priori accurate yield stress predictions beyond the instability point. This fact has important implications when computing the actual forming load for large plastic deformations, as discussed in the following sections.
Remark (ii): It is relevant to mention that the AISI 304 stainless steel is subject to deformation-induced phase transformation of austenite to martensite. The phase transformation mechanisms give rise to complex hardening behaviour according temperature and strain rates. De et al. [13] indicate that the stress-strain curves for low strain rates and temperatures higher than 298 K follow a typical "parabolic" evolution, which, therefore, makes possible to model inelastic deformation using straightforward phenomenological approaches.

3 Alternative Yield Stress Equations and Identification of Material Parameters

It is particularly relevant to acknowledge that phenomenological constitutive models have been largely used (and preferred) in industry. Moreover, many non-logarithmic hardening equations are empirical in nature and have been recommended for individual materials or else portraying specific internal structures (see, for instance, Larour [14] and references therein). However, there have been proposed some yield stress equations derived by using micromechanical concepts that can also be applied within

the realm of phenomenological models. This work considers two non-logarithmic hardening equations which can be obtained from physical mechanisms of dislocation theory and yet recover well-known empirical models (without, however, addressing phase transformation).

El-Magd [15] accounts for physical mechanisms of dislocation theory assuming a Taylor-like correlation between the yield stress and total dislocation density associated with Mecking and Kocks' [16] evolution of the dislocation density. A constant assumption of the micromechanical parameters gives rise to a yield stress equation identical with Voce's [17] empirical relation,

$$\begin{aligned}\sigma_Y &= C_1^v + \left(C_2^v - C_1^v\right)\exp\left(-C_3^v\bar{\varepsilon}_p\right)\\ &= \sigma_0^v + \left(\sigma_\infty^v - \sigma_0^v\right)\left[1 - \exp\left(-\delta^v\bar{\varepsilon}_p\right)\right]\end{aligned}, \tag{4}$$

where $C_1^v = \sigma_\infty^v$ and $C_2^v = \sigma_0^v$ are associated with the saturation and initial yield stress, respectively, and $C_3^v = \delta^v$ represents the deformation rate to approach the saturation stress. Depending upon the material, Voce's equation provides good fit only for small plastic strains owing to the fact that the yield stress asymptotically approaches a constant value for large plastic deformations, i.e. $\sigma_Y \to \sigma_\infty^v$. For instance, El-Magd [15] indicates that Eq. (4) presents acceptable approximations for the austenitic steel X6CrNi18-11 at different temperatures in the range of relatively small strain up to 0.2.

A better representation for larger plastic strains can be derived by approximating the effects of the dislocation storage rate as a linear function of plastic strains [15], so that

$$\begin{aligned}\sigma_Y &= C_1^t + C_4^t\bar{\varepsilon}_p + \left(C_2^t - C_1^t\right)\exp\left(-C_3^t\bar{\varepsilon}_p\right)\\ &= \sigma_0^t + \zeta\,\bar{\varepsilon}_p + \left(\sigma_\infty^t - \sigma_0^t\right)\left[1 - \exp\left(-\delta^t\bar{\varepsilon}_p\right)\right]\end{aligned}, \tag{5}$$

in which $C_1^t = \sigma_\infty^t$ and $C_2^t = \sigma_0^t$ represents the saturation and initial yield stress, respectively, $C_3^v = \delta^t$ is the deformation rate to approach the saturation stress, and $C_4^t = \zeta^t$ portraits the linear hardening coefficient. This equation closely approximates an empirical model proposed by Tome et al. [18]. In addition, hardening laws similar to Eq. (5) have oftentimes been referred as *modified Voce* model. The literature shows increasing use of this hardening equation to describe the yield stress evolution of different materials, such as the 100Cr6 steel [19], X8CrNiMoNb16-16 austenitic steel [15], DP780 and TRIP780 high strength steels [20], and Al-2/4/8/10Si casting alloys [21].

Remark (iii): Voce's and modified Voce hardening equations were not conceived to follow the plastic deformation behaviour naturally represented in the classical logarithmic form. Therefore, this work adopts an optimization strategy to determine parameters of both Eqs. (4) and (5), thereby making possible to evaluate plastic deformation up to final deformation stages (catastrophic failure).

3.1 *Identification of Material Parameters—The Optimization Algorithm*

Parameter identification can also be regarded as an inverse problem, which consists of finding a set of material parameters which minimizes the differences between *experimental measures* and corresponding *computed responses* with respect to a given norm [22]. In the present study, (i) the *experimental measures* comprise loads and displacements evaluated in tensile tests using specimens of different geometry up to macroscopic failure. (ii) The *computed response* is determined by solving an elastic-plastic boundary value problem, which, in this work, is solved by an in-house finite element code based on a hyperelastic, large deformation formulation [23, 24]. (iii) The norm defines how differences are computed and this study adopts a linear combination of the L_2 error norm for each tensile test.

Unconstrained nonlinear optimization is utilised in the present parameter identification problem, which can be generally defined as

$$\begin{aligned} &\text{Minimise} \quad g(\boldsymbol{p}) = \sum_{s=1}^{n_s} \lambda_s g_s(\boldsymbol{p}) \quad \boldsymbol{p} \in R^{n_p} \\ &\text{Such that} \quad p_i^{\inf} \leq p_i \leq p_i^{\sup} \qquad i = 1, \ldots, n_p \end{aligned} \quad , \tag{6}$$

in which $g(\boldsymbol{p})$ is the global objective function (global fitness), computed from individual fitness measures, $g_s(\boldsymbol{p})$, where the subscript "s" indicates a tensile test of an individual type of specimen, and n_s is the total number of specimen types. In Eq. (6), $\boldsymbol{p} = \left[p_1\, p_2 \cdots p_i \cdots p_{n_p}\right]^T$ is the design vector containing n_p design variables p_i (material parameters), and $p_i^{\inf}$ and $p_i^{\sup}$ are lateral limits (minimum and maximum values of each material parameter).

The contribution of the tensile tests of each type of specimen to the global objective function is defined by weights, λ_s, so that $\sum_{s=1}^{n_s} \lambda_s = 1$. The individual fitness, $g_s(\boldsymbol{p})$, is evaluated by the L_2 norm of the differences between the experimental, $\boldsymbol{R}_s^{Exp}$, and corresponding computed loads, $\boldsymbol{R}(\boldsymbol{p})_s^{Num}$, of a tensile test "$s$", as

$$\begin{aligned} g_s(\boldsymbol{p}) &= \left\| \boldsymbol{R}_s^{Exp} - \boldsymbol{R}(\boldsymbol{p})_s^{Num} \right\|_{L_2} \\ &= \sqrt{\sum_{j=1}^{N_s} \left[R_{s,j}^{Exp} - R(\boldsymbol{p})_{s,j}^{Num} \right]^2} \end{aligned} , \tag{7}$$

where N_s is the number of experimental points for tensile test "s". The optimization technique adopted in this work uses the gradient-free downhill simplex method, also known as Nelder-Mead (NM) algorithm [25]. *It is important to mention that other optimization methods could have been used in conjunction with the proposed strategy*. Notwithstanding, the NM algorithm was adopted based on the following reasons:

(i) The NM method does not require a continuously differentiable objective function. The combination of individual objective functions and the high nonlinearity of the plasticity problem can cause the sensitivity analysis (derivative of the global objective function with respect to each design variable) of gradient-based schemes to fail, especially after the maximum load, close to the macroscopic failure (see, for instance, the issues associated with the gradient-based Sequential Quadratic Programming (SQP) method discussed in Vaz Jr. et al. [26]). In the present NM implementation, even if computation of one or more individual fitness, $g_s(\boldsymbol{p})$, fail, the scheme naturally purges the corresponding set of material parameters $\boldsymbol{p}$ and the optimization process continues.

(ii) The NM method was shown competitive in this class of problems when compared to some gradient-based techniques and soft-computing algorithms [27]. The authors discussed application of the Broyden-Fletcher-Goldfarb-Shanno (BFGS), Sequential Quadratic Programming (SQP), Globally Convergent Method of Moving Asymptotes (GCMMA), Particle Swarm Optimization (PSO), Genetic Algorithm (GA), Nelder-Mead and Univariate methods to identification of inelastic parameters using tensile tests and deep drawing operations.

(iii) The Nelder-Mead method has been used successfully in parameter identification associated with more elaborate mechanical tests and complex constitutive relations (which indicates its robustness). For instance, Banabic et al. [28] applied the NM scheme to identification of inelastic parameters for a biaxial tensile test, and Pannier et al. [29] used this optimization method to find elastic-plastic constitutive parameters based on the Virtual Fields Method associated to tensile tests. The NM technique was also successfully used in conjunction with different material constitutive relations, such as composite [30] and damaged [7] materials.

Highlights of the Nelder-Mead algorithm: The NM optimization method defines a regular polytope of $n_p + 1$ vertices (for a n_p-dimensional design space corresponding to a n_p number of material parameters), which moves towards the optimum by replacing the worst vertex by a new one selected from pre-defined positions along a given search direction. The reader is referred to Nelder and Mead [25], Luersen and Le Riche [30], and Lagarias et al. [31] for additional details on the NM optimization technique, and Vaz Jr. et al [26] for the NM algorithm used in the present investigation.

4 Numerical Results and Discussions

The previous sections show that inelastic parameters can be determined using tensile tests based on calibration or inverse problem techniques. The former adopts curve fitting strategies of the true stresses and strains in a $(\ln \sigma) \times (\ln \varepsilon)$ plot, whereas the latter uses optimization methods.

Table 1 Chemical composition of the AISI 304 steel (in wt%)

	Cr	Ni	Mn	Si	C	P	S
Nominal	18–20	8–10.5	max 2.0	max 1.0	max 0.08	max 0.045	max 0.03
This work	18.677	8.780	1.9856	0.21897	0.07612	0.01984	0.02767

Experimental investigations shows that tensile tests of ductile materials involve four general stages: (i) uniform elastic deformation; (ii) plastic deformation under uniform stress states; (iii) instability onset and growth of triaxial stress states; and (iv) catastrophic/macroscopic failure. Calibration procedures are performed under uniaxial stress/strain conditions comprising stage (ii) up to instability onset (or necking) to avoid triaxial stress states. Contrastingly, inverse problem techniques can account for elastic-plastic deformations up to macroscopic failure. This study is performed for the AISI 304 stainless steel with chemical composition presented in Table 1.

In the present work, tensile tests were executed using cylindrical specimens prepared according to the American ASTM E8M-09 [32] and Brazilian ABNT NBR ISO 6892 [33] technical standards under displacement control at room temperature (298 K). Extensometers with initial gauge lengths $l_0 = 25$ mm and $l_0 = 50$ mm were used according to the specimen size with maximum crosshead speed $v_c = 3$ mm/min. The specimens used in this work are illustrated in Fig. 1 and referred as follows:

- ASTM #1: initial gauge length $l_0 = 25$ mm and diameter $d_0 = 6.0$ mm,
- ASTM #2: initial gauge length $l_0 = 50$ mm and diameter $d_0 = 12.54$ mm,
- NBR #3: initial gauge length $l_0 = 50$ mm and diameter $d_0 = 10.0$ mm.

The geometrical models (used in the simulations) for all types of specimens consider axisymmetry around the rotation axis $Z - Z'$ and symmetry about the $R - R'$ axis, making possible to model only 1/4 of the specimen. All cases adopt a structured, eight-noded quadrilateral finite element mesh with 200 elements and 661 nodes with progressive refinement towards the specimen $R - R'$ axis. The finite element mesh used for specimen ASTM #2 is presented in Fig. 2. Meshes for ASTM #1 e NBR #3 specimens are geometrically proportional to ASTM #2 with identical element topology. The Young modulus and Poisson's ratio used in the simulations are $E = 205$ GPa and $\nu = 0.29$, respectively.

4.1 Curve Fitting of Logarithmic-Type Yield Stress Curves

The curve fitting procedure for the Swift (Eq. 1), double-n Swift (Eq. 2) and third-order logarithmic curves (Eq. 3) requires definition of lower and upper limits, i.e. the *elastic limit* and *instability onset*, respectively. The elastic limit corresponds to the lower bound imposed by the elastic curve, $\sigma = E\varepsilon$, whereas the maximum load was assumed as the instability limit. The true strains and true stresses are determined as $\varepsilon = \ln(1 + e)$ and $\sigma = S(1 + e)$, respectively, where $e = \Delta l / l_0$ is the elongation

(a) Specimen *ASTM #1*: $l_0 = 25$ mm, $d_0 = 6$ mm.

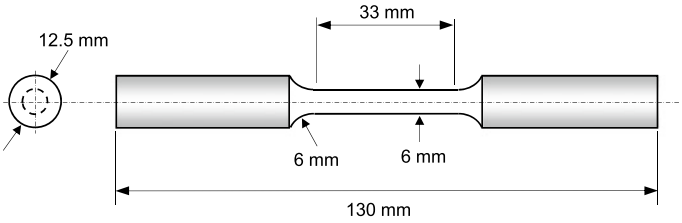

(b) Specimen *ASTM #2*: $l_0 = 50$ mm, $d_0 = 12.54$ mm.

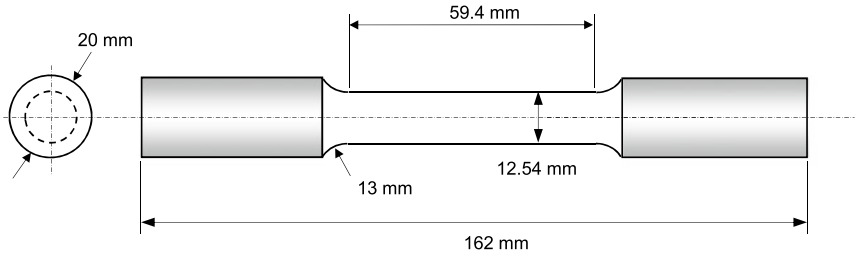

(c) Specimen *NBR #3*: $l_0 = 50$ mm, $d_0 = 10$ mm.

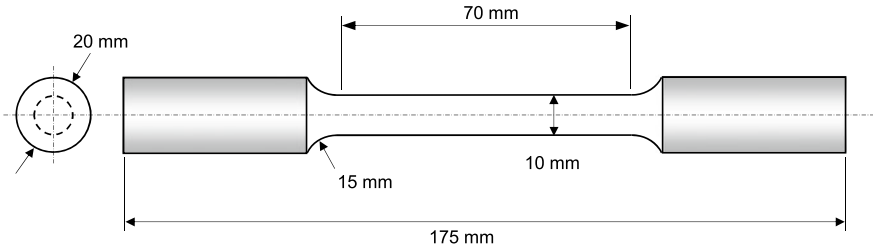

Fig. 1 Geometry of the specimens for the ASTM and ABNT-NBR standards

Fig. 2 Finite element mesh for the *ASTM #2* specimen

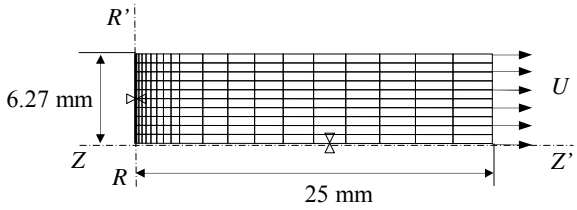

(engineering strain), $S = R/A_0$ is the engineering stress, R is the axial load, and A_0 is the initial cross-sectional area [8]. It was observed that evolution of the true stress−true strain curve for the ASTM #1, ASTM #2 and NBR #3 specimens presents small variations up to instability onset. Such results indicate a good consistency of the measured data. *Therefore, curve fitting was performed taking into account the true stress–true strain data of all types of specimens, making possible to determine a single set of parameters for each hardening curve, i.e. Swift, double-n Swift and cubic logarithmic curves*.

Figure 3 shows the experimental data and fitted equations in a $(\ln \sigma) \times (\ln \varepsilon)$ plot, and Table 2 presents the corresponding material parameters. For the sake of clarity, not all experimental points are represented in Fig. 3 and forthcoming figures. The best fit was achieved by the cubic logarithmic curve with a coefficient of determination $R^2 = 0.998627$, as represented in Fig. 3 by the thick solid line. The double-n Swift yield stress curve was also able to provide a good approximation to the experimental values with a mean coefficient of determination $\overline{R}^2 = 0.979821$ (solid line in Fig. 3). On the other hand, the Swift curve provided a very poor fitting, clearly indicated by the dashed line in Fig. 3, with a coefficient of determination $R^2 = 0.948860$.

Numerical simulations of the tensile test were conducted for the ASTM #1, ASTM #2 and NBR #3 specimens using the geometrical models previously described. The maximum experimental displacements measured for each specimen are applied to the corresponding geometrical model as: [ASTM #1 ($l_0/2 = 12.5$ mm): $U_{\#1} = 7.30$ mm], [ASTM #2 ($l_0/2 = 25$ mm): $U_{\#2} = 12.88$ mm], and [NBR #3 ($l_0/2 = 25$

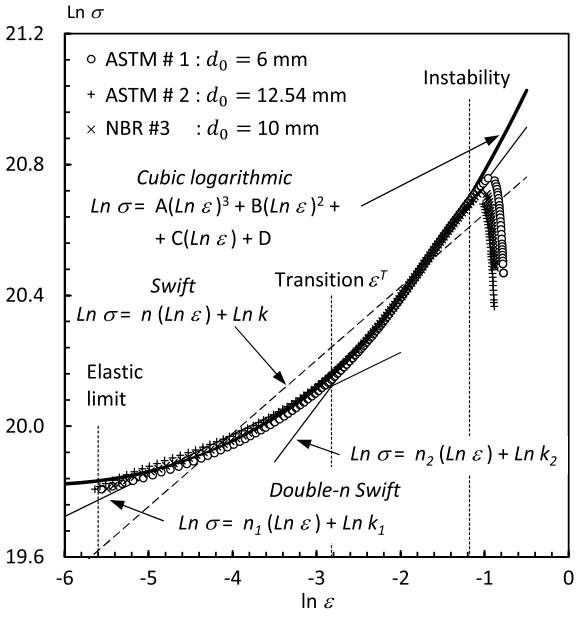

Fig. 3 Curve fitting of the true stresses and strains for the Swift, double-n Swift and cubic logarithmic hardening equations

Table 2 Material parameters for the Swift, double-*n* Swift and cubic logarithmic hardening equations

Model	Parameter	Value
Swift	k	1162.60 kPa
	n	0.223907
	ε_0	1.27526×10^{-3}
Double-*n Swift*	k_1	781.201 kPa
	n_1	0.125434
	k_2	1436.36 kPa
	n_2	0.341271
	ε_0	1.71422×10^{-3}
	ε_p^T	5.95026×10^{-3}
Cubic logarithm	A	3.59939×10^{-3}
	B	8.17363×10^{-2}
	C	0.608688
	D	21.3109
	ε_0	1.97856×10^{-3}

mm): $U_{\#3} = 12.80$ mm]. The material parameters presented in Table 2 for the Swift, double-*n* Swift and cubic logarithmic equations were used in the simulations.

Figure 4a–c present the loading curves for specimens ASTM #1, ASTM #2 and NBR #3, respectively, computed using Swift, double-*n* Swift and cubic logarithmic models. The poor fitting exhibited by the Swift curve (see the dashed line in Fig. 3) is translated into also poor numerical loading response for all specimens: the tensile load is overestimated for small strains and grossly underestimated for large deformations, i.e. the excessive necking towards the end of the tensile test caused an unrealistic decrease of the tensile load. The best data fitting demonstrated by the cubic logarithmic curve is strictly observed up to the maximum load for all specimens (thick solid lines in Fig. 4). However, the hardening parameters of the cubic logarithmic curve obtained for the present tensile tests caused the computed tensile load to steadily increase after the maximum experimental load, i.e. no necking was observed in the simulations up to the maximum applied displacements ($U_{\#1}$, $U_{\#2}$ and $U_{\#3}$) for the respective specimens.

The fitted double-*n* Swift equation provides the best results for the tensile load. Such good approximation (up to the maximum load) for stainless steels has already been established in the literature [10–12]. Figure 4a and c show that this hardening equation was also able to capture the general tendency of the load behaviour after the maximum load. Notwithstanding, the transition between the different slopes of the double-*n* Swift curve (represented by the hardening coefficients n_1 and n_2, as shown in Fig. 3) caused an unrealistic bulge in the loading curve when the elongation approaches $\varepsilon^T \approx 0.06314$ (i.e. when plastic strains approximate ε_p^T), as highlighted in Fig. 5. The maximum differences between experimental and numerical loads in the transition region of the double-*n* Swift curve increase with the cross-sectional area, so that $\Delta R_{\#1} \approx 310$ N ($d_0 = 6$ mm), $\Delta R_{\#3} \approx 1200$ N ($d_0 = 10$ mm), and $\Delta R_{\#2} \approx 2700$ N ($d_0 = 12.54$ mm) for specimens ASTM #1, NBR #3, and ASTM #2, respectively.

(a) ASTM #1 : $d_0 = 6$ mm. (b) ASTM #2 : $d_0 = 12.54$ mm. (c) NBR #3 : $d_0 = 10.00$ mm

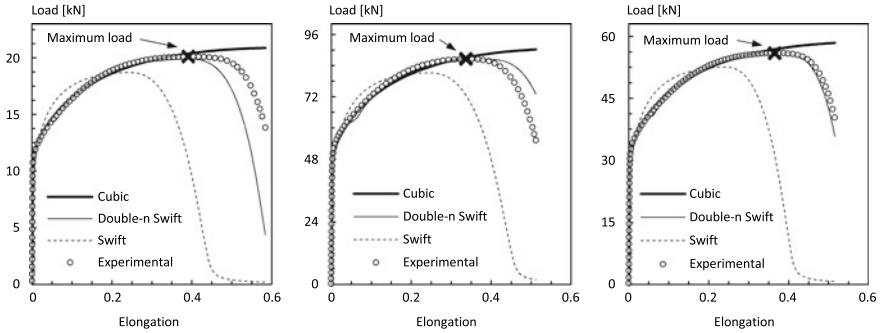

Fig. 4 Loading curve for specimens ASTM #1, ASTM #2 and NBR #3: logarithmic-based yield equations

Fig. 5 Loading curves for the *double-n Swift* curve

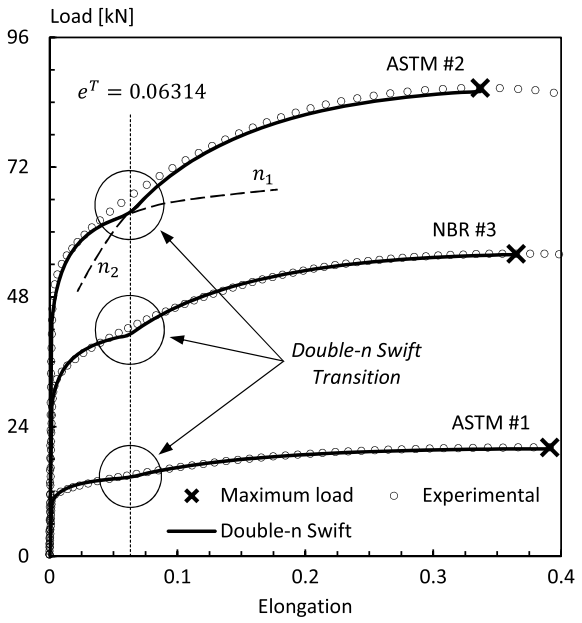

Remark (iv): the curve-fitting strategy to determine the hardening parameters for the Swift, double-*n* Swift and cubic logarithmic equations minimizes the differences between experimental and numerical true strains and true stresses based on polynomial least square regression for a $(\ln \sigma) \times (\ln \varepsilon)$ plot. This strategy does not require information *after* the upper limit given by the maximum load. Therefore, it is not expected, a priori, a good approximation of the loading curve for the logarithmic-based hardening equations after necking onset under triaxial stress states.

4.2 Parameter Identification of Alternative Yield Stress Equations

The strategy used to determine the hardening parameters of Voces (Eq. 4) and modified Voce (Eq. 5) yield equations is markedly different from calibration procedures. Instead of using curve fitting techniques, material parameters of both equations are determined by numerically assessing the load response of the specimens submitted to controlled displacements. The final hardening parameters are those which minimize compound differences (evaluated by the L_2 norm) between experimental and numerical loads for specimens ASTM #1, ASTM #2 and NBR #3. The Nelder-Mead optimization algorithm was used in the simulations, which requires an initial estimate of the material parameters, $\boldsymbol{p}_i^{(0)}$, and corresponding minimum and maximum values (lateral constraints, $p_i^{\inf}$ and $p_i^{\sup}$), as indicated in Table 3. For the sake of objectivity, assessment of the capacity of the algorithm to solve the problem and other studies of the optimization scheme are omitted here (e.g. convexity, sensitivity to mesh size and to changes of the initial estimates and lateral constraints, influence of the convergence limit, etc.). It is also relevant to emphasise that equal contribution for tensile tests of each specimen ASTM #1, ASTM #2 and NBR #3 was assumed in the identification process, so that $\lambda_1 = \lambda_2 = \lambda_3 = 1/3$ in Eq. (6).

The material parameters determined for the original Voce and modified Voce hardening equations are presented in Table 3, whereas the loading curves for the tensile test of each specimen are shown in Fig. 6. The simulations indicate that both hardening models present good approximation to the experimental data up to the maximum load. Nevertheless, evaluation of the loading curves of all specimens indicates that the modified Voce equation was able to provide a better prediction than the Voces model. It is possible to visually identify in Fig. 6a that, for the smallest specimen ASTM #1 ($d_0 = 6$ mm), the original Voce equation led to large differences towards the end of the loading process. Quantification of such differences is discussed in the following paragraph.

A comparative (quantitative) assessment with respect to load evolution for hardening equations associated with both curve-fitting (Swift, double-*n* Swift and cubic

Table 3 Lateral constraints, initial estimates and final hardening parameters for the *Voce* and *modified Voce* hardening equations

Model	Parameter	$p_i^{\inf}$	$p_i^{\sup}$	$\boldsymbol{p}_i$	Value
Voce Eq. (4)	σ_0^v (MPa)	200	800	500	432.137
	σ_∞^v (MPa)	400	1500	800	1424.73
	δ^v	0	50	25	2.46965
Modified Voce Eq. (5)	σ_0^t (MPa)	200	800	500	406.749
	σ_∞^t (MPa)	400	1200	800	768.524
	ζ^t (MPa)	300	1200	750	746.444
	δ^t	0	50	25	7.04351

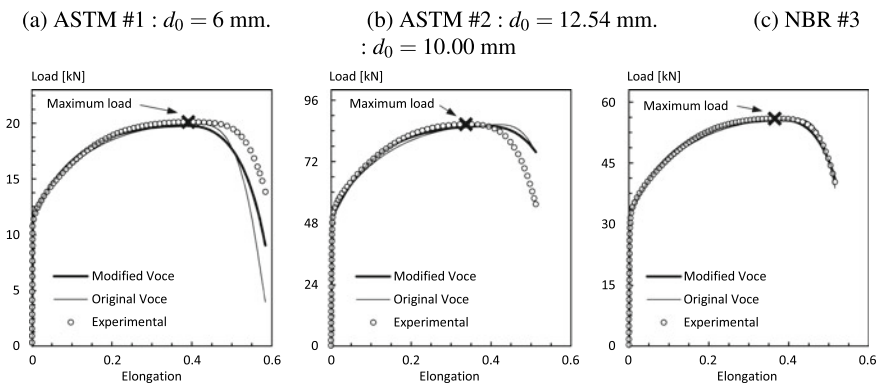

Fig. 6 Loading curve for specimens ASTM #1, ASTM #2 and NBR #3: original Voce and modified Voce yield equations

polynomial) and inverse problem (Voce and modified Voce) techniques was also performed. In order to better perceive eventual discrepancies, specimen-based, $\varphi_s(\boldsymbol{p})$, and global, $\Phi(\boldsymbol{p})$, indices were defined based on the relative L_2 error norm between experimental and numerical tensile loads as

$$\varphi_s(\boldsymbol{p}) = \frac{\left\| \boldsymbol{R}_s^{Exp} - \boldsymbol{R}_s^{Num} \right\|_{L_2}}{\left\| \boldsymbol{R}_s^{Exp} \right\|_{L_2}} \quad \text{and} \quad \Phi(\boldsymbol{p}) = \sum_{s=1}^{3} \varphi_s(\boldsymbol{p}). \tag{8}$$

Table 4 presents both $\varphi_s(\boldsymbol{p})$ and $\Phi(\boldsymbol{p})$, from which one can conclude that the modified Voce equation presents the best global performance, followed by the double-n Swift, original Voce, cubic logarithmic and Swift equations. Noticeably, the global error measure $\Phi(\boldsymbol{p})$ for the modified Voce equation is 30% smaller than the double-n Swift. Table 4 also indicates that differences change for individual specimens, with the modified Voce equation attaining best approximations for ASTM #1 and NBR #3 specimens and the double-n Swift for the ASTM #2 specimen. Figure 7 enables a visual appraisal of the differences between the loading curves for the modified Voce and double-n Swift hardening equations. The relative large differences exhibited by the double-n Swift loading curve after the maximum load for specimens ASTM #1 and NBR #3 (clearly visible in Fig. 7) led to the larger values of the global index, $\Phi(\boldsymbol{p})$. It can also be observed in Fig. 7 and Table 4 that differences for the ASTM #2 specimen are marginal for both hardening equations.

Remark (v): Some reasons might explain the better performance of the modified Voce hardening equation with respect to the double-n Swift model: (i) the optimization technique (minimization of the experimental-numerical differences) utilised for the modified Voce equation accounts for the experimental loading curve up to macroscopic failure, which contrasts to the double-n Swift model that performs curve fitting up to the maximum load. (ii) The unrealistic bulge located in the transition between hardening indices n_1 and n_2 imposes further differences for the double-n Swift equa-

Table 4 Individual, $\varphi_s(\boldsymbol{p})$, and global, $\Phi(\boldsymbol{p})$, error indices for all hardening equations

Technique	Hardening model	$\varphi_s(\boldsymbol{p})$			$\Phi(\boldsymbol{p})$
		ASTM #1	ASTM #2	NBR #1	Global index
Curve fitting	*Swift*	0.5184282	0.4239484	0.4881430	1.430520
	Double-n Swift	0.1481382	**0.0735302**	0.0249953	0.246664
	Cubic logarithmic	0.0981038	0.1419500	0.0900999	0.330154
Optimization	*Original Voce*	0.1498700	0.0871119	0.0161115	0.253093
	Modified Voce	**0.0825237**	0.0805894	**0.0108542**	**0.173967**

The bold value indicates the minimum values of the error indices

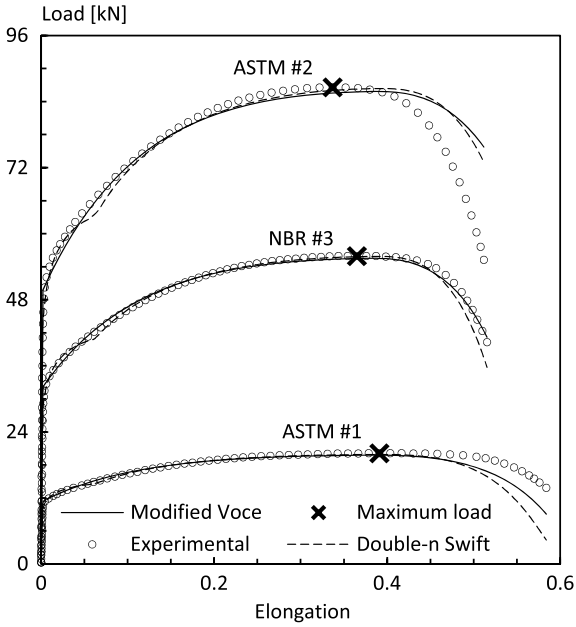

Fig. 7 Loading curve for *double-n Swift* and *modified Voce* hardening equations

tion. (iii) No physical justification holds for double-*n* Swift model since this equation if essentially of empirical character.

5 Concluding Remarks

Austenitic stainless steels have been used in many applications, ranging from consumer items (cutlery, pans, sinks, etc.) and architectural components (ornamental work, decorative panels, poolside fittings and fixings, etc.) to industrial equipment (e.g. pharmaceutical, food and beverage, chemical and mining equipment). The stainless steel AISI 304 constitutes the most used grade owing to its combination of good corrosion/oxidation resistance, weldability, formability, toughness characteris-

tics and ductility (large deformation before failure onset). Due to such high industrial interest, this work discusses suitability of some selected equations to model hardening evolution and alternative strategies to obtain the corresponding parameters within the phenomenological framework.

Tensile tests have long been used to determine hardening parameters of ductile materials. Aiming to confer further credibility to the present analysis, specimens prepared according to the American ASTM E8M-09 [32] (ASTM #1 and ASTM #2) and Brazilian ABNT NBR ISO 6892 [33] (NBR #3) standards were used. Due to simplicity, calibration procedures based on curve-fitting strategies are by far the most common approach adopted to determine hardening parameters. The main drawback of this technique is the requirement of uniform deformation, which restricts its application to relatively small plastic deformations (up to instability onset). This work addresses this method by comparing the following logarithmic-type hardening equations: *Swift* [9] (largely used in industry), *double-n Swift* (previously recommended for austenitic steels [10–12]), and a *3rd order* $(\ln \sigma) \times (\ln \varepsilon)$ *polynomial equation* (recommended for some DP and TRIP steels [6]). The latter provided the best fit of the experimental data up to maximum load, followed by the *double-n Swift* and *Swift* models.

Simulation of metal forming processes, such as extrusion, wire drawing and deep drawing, involves larger plastic deformations than those permitted by curve-fitting strategies. Therefore, this study also addresses identification of material parameters based on inverse problem techniques (by using optimization methods). In such case, *Voce*'s and *modified Voce* equations were adopted to describe material hardening. Despite of phenomenological character, these equations were selected due to their association with physical mechanisms of the dislocation theory.

A comparative assessment of all hardening equations (*Swift, double-n Swift, 3rd order logarithmic, Voce* and *modified Voce*) were performed by numerical simulation of tensile tests for the ASTM #1, ASTM #2 and NBR #3 specimens up to macroscopic failure. The computational model uses an in-house fine element code based on an elastic-plastic, finite strain formulation [23, 24]. The experimental data shows relevant plastic deformation after the maximum load, reaching elongations (engineering strains) up to 50% higher than those observed for uniform deformation. In order to quantify the approximation provided by the aforementioned hardening equations and corresponding parameters, an index was defined based on the relative L_2 error norm between experimental and numerical loads up to macroscopic failure. The simulations indicate that the *modified Voce* equation produced an error index 30% smaller than the *double-n Swift*. Moreover, both equations were able to predict the load behaviour after the instability onset with acceptable accuracy. Contrastingly, *Swift*'s hardening model grossly underestimates tensile loads after maximum load, whereas no instability onset was predicted by the *3rd order polynomial* equation.

Therefore, owing to the discussion summarised in the previous paragraphs, the *modified Voce* equation associated with inverse problem techniques based on optimization methods are recommended to describe isothermal hardening for the austenitic stainless steel AISI 304. The *double-n Swift* equation can also be used, but some care should be exercised.

Acknowledgements The authors acknowledge the financial support provided by the Brazilian funding agency CNPq (National Council for Scientific and Technological Development), Grant no. 303412/2016-0.

References

1. McGuire MF (2008) Stainless steels for design engineers. ASM, Materials Park
2. Subramonian S, Kardes N (2012) Materials for Sheet Forming. In: Altan T, Tekkaya E (eds) Sheet Metal Forming: Fundamentals. ASM, Materials Park
3. Samuel KG, Rodriguez P (2005) On power-law type relationships and the Ludwigson explanation for the stress-strain behaviour of AISI 316 stainless steel. J Mater Sci 40:5727–5731
4. Samuel KG (2006) Limitations of Hollomon and Ludwigson stress strain relations in assessing the strain hardening parameters. J Phys D: Appl Phys 39:203–212
5. Ponthot JP, Kleinermann JP (2006) A cascade optimization methodology for automatic parameter identification and shape/process optimization in metal forming simulation. Comput Meth Appl Mech Eng 195:5472–5508
6. Dimatteo A, Colla V, Lovicu G, Valentini R (2015) Strain hardening behavior prediction model for automotive high strength multiphase steels. Steel Res Int 86:1574–1582
7. Vaz M Jr, Muoz-Rojas PA, Cardoso EL, Tomiyama M (2016) Considerations on parameter identification and material response for Gurson-type and Lemaitre-type constitutive models. Int J Mech Sci 106:254–265
8. Davis JR (2004) Tensile testing, 2nd edn. ASM, Materials Park
9. Swift HW (1952) Plastic instability under plane stress. J Mech Phys Solids 1:1–18
10. Hertelé S, De Waele W, Denys R (2011) A generic stress strain model for metallic materials with two-stage strain hardening behaviour. Int J Non-linear Mech 46:519–531
11. Kashyap BP, McTaggart K, Tangri K (1988) Study on the substructure evolution and flow behaviour in type 316L stainless steel over the temperature range 21–900 °C. Phil Mag A 57:97–114
12. Kashyap BP, Tangri K (1995) On the Hall-Petch relationship and substructural evolution in type 316L stainless steel. Acta Metall Mater 43:3971–3981
13. De AK, Speer JG, Matlock DK et al (2006) Deformation-induced phase transformation and strain Hardening in type 304 austenitic stainless steel. Metall Mater Trans A 37A:1875–1886
14. Larour P (2010) Strain rate sensitivity of automotive sheet steels: influence of plastic strain, strain rate, temperature, microstructure, bake hardening and pre-strain. Dr.-Ing. Dissertation, RWTH Aachen
15. El-Magd E (2004) Modeling and Simulation of Mechanical Behavior. In: Totten GE, Xie L, Funatani K (eds) Modeling and Simulation of Material Selection and Mechanical Design. Dekker, New York
16. Mecking H, Kocks UF (1981) Kinetics of flow and strain hardening. Acta Metall 29:1865–1875
17. Voce E (1948) The relationship between stress and strain for homogeneous deformation. J Inst Metals 74:537–562
18. Tome C, Canova GR, Kocks UF et al (1984) The relation between macroscopic and microscopic strain hardening in f.c.c. polycrystals. Acta Metall 32:1637–1653
19. Gruber M, Lebaal N, Roth S et al (2016) Parameter identification of hardening laws for bulk metal forming using experimental and numerical approach. Int J Mater Form 9:21–33
20. Panich S, Barlat F, Uthaisangsuk V, Suranuntchai S, Jirathearanat S (2013) Experimental and theoretical formability analysis using strain and stress based forming limit diagram for advanced high strength steels. Mater & Design 51:756–766
21. Sugio K, Sasaki G, Tabata J, Fuyama N, (2017) In: Proceedings of the International Symposium on Green Manufacturing and Application. The Korean Society for Precision Engineering, Seoul, pp 51–53

22. Vaz M Jr, Cardoso EL, Stahlschmidt J (2013) Particle swarm optimization and identification of inelastic material parameters. Eng Comput 30:936–960
23. de Souza Neto EA, Peric D, Owen DRJ (2008) Computational Methods for Plasticity: Theory and Applications. Wiley, Chichester
24. Vaz M Jr, Lange MR (2017) Thermo-mechanical coupling strategies in elasticplastic problems Continuum Mech. Thermodyn. 29:373–383
25. Nelder JA, Mead R (1965) A simplex method for function minimization. Comput J 7:308–313
26. Vaz M Jr, Luersen MA, Muoz-Rojas PA, Trentin RG (2016) Identification of inelastic parameters based on deep drawing forming operations using a globallocal hybrid Particle Swarm approach. C R Mecanique 344:319–334
27. Vaz M Jr, Cardoso EL, Muñoz-Rojas PA et al (2015) Identification of constitutive parameters − optimization strategies and applications. Mat-wiss Werkstofftech 46:477–491
28. Banabic D, Kuwabara T, Balan T et al (2003) Non-quadratic yield criterion for orthotropic sheet metals under plane-stress conditions. Int J Mech Sci 45:797–811
29. Pannier Y, Avril S, Rotinat R, Pierron F (2006) Identification of elasto-plastic constitutive parameters from statically undetermined tests using the virtual fields method. Exp Mech 46:735–755
30. Luersen MA, Le Riche R (2004) Globalized NelderMead method for engineering optimization Comput & Struct 82:2251–2260
31. Lagarias JC, Reeds JA, Wright MH, Wright PE (1998) Convergence properties of the Nelder-Mead simplex method in low dimensions. SIAM J Optim 9:112–147
32. ASTM E8, E8M–09, (2009) Standard Test Methods for Tension Testing of Metallic Materials. ASTM International, West Conshohocken
33. ABNT NBR-ISO 6892, (2002) Metallic materials − Tensile testing at ambient temperature. ABNT, Rio de Janeiro